Theory of semiconductor quantum-wire-based single- and two-qubit gates

Tobias Zibold and Peter Vogl

Walter Schottky Institute, Technische Universität München, 85748 Garching, Germany

Andrea Bertoni

CNR-INFM National Research Center on NanoStructures and BioSystems at Surfaces (S3), 41100 Modena, Italy

A GaAs/AlGaAs based two-qubit quantum device that allows the controlled generation and straightforward detection of entanglement by measuring a stationary current-voltage characteristics is proposed. We have developed a two-particle Green's function method of open systems and calculate the properties of three-dimensional interacting entangled systems nonperturbatively. We present concrete device designs and detailed charge-self-consistent predictions. One of the qubits is an all-electric Mach-Zehnder interferometer that consists of two electrostatically defined quantum wires with coupling windows, whereas the second qubit is an electrostatically defined double quantum dot located in a second two-dimensional electron gas beneath the quantum wires. We find that the entanglement of the device can be controlled externally by tuning the tunneling coupling between the two quantum dots.

PACS number(s): 73.23.−b, 73.63.Nm, 03.67.Mn

I. INTRODUCTION

Semiconductor based concepts for quantum information processing promise a high degree of scalability. However, the implementation of even a single qubit proves to be more difficult in semiconductors than in alternative approaches.[1–7] The reasons lie in the short decoherence times and strong interactions between elementary excitations in solids.[8] While a seven-qubit NMR quantum computer was realized already in 2001,[9] the first two-qubit quantum operation in semiconductors has been demonstrated with spin qubits only recently.[10–12]

At liquid helium temperatures and below, electrons in a GaAs/AlGaAs two-dimensional electron gas (2DEG) show mean free paths as well as phase-relaxation lengths of the order of $10-20$ μm, which are remarkably long distances.[13] Indeed, Bertoni *et al.*[14] and Ionicioiu *et al.*[15] have proposed a scheme for quantum computation in semiconductors that exploits these long coherence lengths for electrons propagating through quantum wires (QWRs). In this scheme, a single electron propagates through two parallel QWRs that represent the qubit states $|0\rangle$ and $|1\rangle$, respectively. A single-qubit rotation gate can be realized by an electronic directional coupler[16,17] that may consist of a small window in the barrier between the two QWRs and is able to transfer the wave packet from one channel to the other. Single-qubit structures have been studied theoretically by several authors[18–21] who showed how the dimensions of the coupling window can be utilized to tailor the transfer process. This approach allows one, at least in principle, to apply multiple quantum gate operations to a qubit without exceeding the relevant coherence lengths.

Universal quantum computation requires not only one-qubit but also two-qubit gates[6] that are responsible for the creation of entanglement between the qubits. To this end, two pairs of QWRs may be brought close to one another so that the electrons in the QWRs can interact with one another in a controlled way via their Coulomb repulsion. This concept has been analyzed both for wave packets[22–25] as well as for stationary states.[20,26,27] The latter investigations used simple models that provide important proofs of principle but do not provide quantitative predictions of realizable device structures that exhibit quantum gate operations.

While two-qubit devices have only been addressed theoretically in the literature, one-qubit systems have also stimulated a number of experiments in both lateral[28,29] as well as vertical[30,31] nanostructures. However, quantum entanglement can not clearly be exposed in single-qubit systems as entanglement expresses the nonseparability of a multiqubit state. Therefore, the following step toward the realization of a prototype quantum gate based on coupled QWRs consists of a two-qubit device. Also, we should keep in mind that conceivable two-qubit experiments need realistic estimations of an entanglement witness that is experimentally accessible and a clear signature of the correct coherent functioning of the directional coupler.

The aim of the present work is to theoretically study realistic single- and two-qubit quantum gates by proposing conceptually simple and experimentally realizable semiconductor devices for quantum information processing. The system proposed is based on ballistic GaAs/AlGaAs QWRs and allows for the controlled generation and detection of entanglement between an all-electric Mach-Zehnder interferometer and an electrostatically defined single-electron double quantum dot. The Mach-Zehnder interferometer is realized by two electrostatically defined QWRs that are connected by two coupling windows. We model the electrons that are propagating through the interferometer by stationary scattering states, and our qubit state will be defined accordingly. In fact, the original proposal of Bertoni *et al.* involves the injection of electron wave packets into the pair of QWRs. However, we chose here a time-independent approach since (i) it is equivalent to the time-dependent one when the spatial dimension of the wave packet tends to be larger than the device (indeed, this is the case in our devices due to the small source and/or drain biases leading to a well defined kinetic energy of the electron), (ii) the structures that implement the quantum gates operate in the same way, and (iii) it

allows us to compute realistic estimations of the charge-self-consistent ballistic I-V characteristics of the device.

In our calculations, we include the detailed charge-self-consistent three-dimensional device geometry, material composition, doping profile, and bias voltage. Importantly, we demonstrate that the all-electric Mach-Zehnder interferometer can function as a fully controllable single-qubit gate for experimentally attainable parameters. In addition, we have developed a Green's function method for the quantitative analysis of the entangled Mach-Zehnder and double quantum dot system that includes the Coulomb interaction between the two qubits nonperturbatively. In order to gain better qualitative insight into the numerical results, we interpret them in terms of an analytical model that reproduces the computational results qualitatively. Taking both results together, we are able to show that the degree of entanglement can be related to the dc I-V characteristics of the interferometer and that the Mach-Zehnder double quantum dot device can be employed as an externally controllable two-qubit gate.

This paper is organized as follows. In Sec. II, we introduce a method for the quantum-mechanical calculation of the ballistic current through an interacting two-particle system. This includes the calculation of the electronic structure and the determination of the ballistic transmission characteristics of the realistic three-dimensional nanostructure. In Sec. III, we discuss numerical details of the method. In Sec. IV, we introduce a simplified analytical scheme able to gather the essential features of the two-qubit device. The results obtained with this approach will be compared, in the following section, with the calculations of the realistic device. Section V focuses on the results and the discussion of the ballistic current through the proposed GaAs/AlGaAs single- and two-qubit QWR devices. In the same section, the degree of entanglement between the two qubits is evaluated. The paper concludes with final remarks and a summary in Sec. VI.

II. METHOD

In this section, we present a method for the calculation of the stationary ballistic current of two interacting particles in realistic three-dimensional nanostructures. We restrict ourselves to the case where only one of the two particles (say, particle 1) contributes to the current while the second particle (particle 2) is assumed to be bound. Importantly, this method accounts for many-particle effects nonperturbatively, which is an important prerequisite of studying entanglement and, consequently, predicting solid-state based quantum information processing. The presently developed scheme generalizes the contact block reduction (CBR) method for single-particle ballistic currents that we have developed previously.[33,34] In analogy to the CBR method, we proceed in two steps that we will describe in this section. First, we determine the equilibrium electronic structure of a closed two-particle system, obtained by substituting the leads of our device with closed boundary conditions. Then, in the second step, we calculate the current-carrying states of the open two-particle system. In fact, the closed calculation only provides a convenient basis for the computation of the scattering states. For the sake of efficiency and without loss of generality, we perform the former calculation in the Hartree approximation by solving two coupled Schrödinger and Poisson equations. Then, we use single-particle product states as the basis for the scattering states of the fully interacting two-particle device.

A. Electronic structure of particle 1

We consider a single-particle, single-band, effective mass Schrödinger equation for this electron and include the electrostatic Hartree potential in the absence of the second particle. The closed system is represented by a Hermitian Hamiltonian with von Neumann boundary conditions for the wave functions at the contacts (vanishing normal derivative).[33,34] The electronic structure of the closed device is calculated self-consistently. To this end, we iteratively solve the Schrödinger equation

$$H_1\langle\mathbf{x}|\alpha_i\rangle = \left[-\frac{\hbar^2}{2m}\nabla\frac{1}{m^*(\mathbf{x})}\nabla + E_c(\mathbf{x}) - e\phi(\mathbf{x})\right]\langle\mathbf{x}|\alpha_i\rangle$$
$$= E_i^0\langle\mathbf{x}|\alpha_i\rangle, \qquad (1)$$

and the nonlinear Poisson equation

$$\nabla\varepsilon_r(\mathbf{x})\varepsilon_0\nabla\phi(\mathbf{x}) = -e\rho[\phi], \qquad (2)$$

until the electrostatic potential ϕ and the total charge density ρ have reached convergence. The effective mass m^*, the conduction band offset E_c, and the relative dielectric constant ε_r are position-dependent material parameters in a general three-dimensional nanostructure that may be composed of several different materials. The total charge density is composed of the electron density $n(\mathbf{x})$ and the ionized donor density $N_D^+(\mathbf{x})$,

$$\rho(\mathbf{x}) = -n(\mathbf{x}) + N_D^+(\mathbf{x}). \qquad (3)$$

The latter results from the donor density $N_D(\mathbf{x})$, the degeneracy g_D, and the donor energy E_D according to the Thomas-Fermi approximation,

$$N_D^+(\mathbf{x}) = \frac{N_D(\mathbf{x})}{1 + g_D e^{(E_F - E_D)/k_B T}}. \qquad (4)$$

The electron density is calculated quantum mechanically by occupying the electronic states according to the Fermi-Dirac statistics,

$$n(\mathbf{x}) = \sum_i |\langle\mathbf{x}|\alpha_i\rangle|^2 f\left(\frac{E_i^0 - E_F}{k_B T}\right). \qquad (5)$$

Here, T denotes the temperature, k_B is Boltzmann's constant, E_F denotes the Fermi level, and f is the Fermi distribution function.

B. Electronic structure of particle 2

For the second particle, we will focus on an electron in a closed double quantum dot that can tunnel between these dots. The two lowest lying quantum states can be described by an effective Hamiltonian that takes into account the energy splitting Δ between the ground states of the isolated

quantum dots and the tunneling coupling t between the two quantum dots. This 2×2 Hamiltonian is given by

$$H_2|Y\rangle = \begin{pmatrix} -\dfrac{\Delta}{2} & -\dfrac{t}{2} \\[2mm] -\dfrac{t}{2} & \dfrac{\Delta}{2} \end{pmatrix} |Y\rangle = E_Y|Y\rangle. \qquad (6)$$

Typical values for Δ and t for lateral semiconductor quantum dots are of the order of 10 μeV.[35] We use this model Hamiltonian for the subsystem of the second particle and represent the charge distribution of the electron in the ground state of each (isolated) quantum dot by a point charge centered at $\mathbf{x}_0$ and $\mathbf{x}_1$, respectively. The use of a model Hamiltonian rather than a realistic three-dimensional device Hamiltonian is not a principle limitation of the present method but is adequate for the concrete device geometry that we will study in detail in this paper. The eigenstates of H_2 are linear combinations of the ground states $|0\rangle$ and $|1\rangle$ of the two isolated quantum dots,

$$|B\rangle = h_{B0}|0\rangle + h_{B1}|1\rangle, \qquad (7)$$

$$|A\rangle = h_{A0}|0\rangle + h_{A1}|1\rangle, \qquad (8)$$

with real valued coefficients h_{YJ} ($Y=A,B$, $J=0,1$). Here, $|B\rangle$ is the bonding eigenstate and $|A\rangle$ the antibonding eigenstate. The corresponding eigenenergies are

$$E_B = -\frac{1}{2}\sqrt{t^2 + \Delta^2}, \qquad (9)$$

$$E_A = \frac{1}{2}\sqrt{t^2 + \Delta^2}. \qquad (10)$$

For vanishing t, the eigenstates $|B\rangle$ and $|A\rangle$ reduce to $|0\rangle$ and $|1\rangle$.

C. Interaction matrix elements

The Coulomb interaction V_{12} between particles 1 and 2 yields the following expression for the interaction matrix elements:

$$\langle \alpha_i Y | V_{12} | \alpha_j Z \rangle = \frac{e^2}{4\pi\varepsilon_r\varepsilon_0} \int d^3x \langle \alpha_i|\mathbf{x}\rangle\langle\mathbf{x}|\alpha_j\rangle \sum_{J=0,1} \frac{h_{YJ}h_{ZJ}}{|\mathbf{x}-\mathbf{x}_J|}, \qquad (11)$$

where $|\alpha_i Y\rangle$ is the product state of particle 1 state $|\alpha_i\rangle$ and particle 2 state $|Y\rangle$.

D. Ballistic transport through a system of two interacting particles

In this second step, we develop a Green's function method by extending the CBR method[33,34] to the case of an open device that describes a system of two interacting particles. We stress that we will consider the two particles as distinguishable. This is not an approximation for the proposed two-qubit devices but comes directly from the system geom-

etry. Indeed, we choose the QWRs and the double dot to be well separated from each other so that no significant tunneling between the two structures can occur. In other words, the two wave functions, namely, the bound state in the double dot and the scattering state in the QWRs, never overlap. This leads to the distinguishability of the two particles based on their spatial localization. In addition, we assume that the interaction is negligible outside the device due to screening in the contacts and/or due to barriers. In the following, the term *device* denotes a finite three-dimensional region that is coupled to reservoirs by an arbitrary number of leads. The device may be under applied bias and contain some spatially varying potential. The total (two-particle) Hamiltonian of the system, including the device and the leads, can be written in symbolic matrix form as

$$H_{\text{tot}} = \begin{pmatrix} H_1^L & 0 & 0 & W_1 \\ 0 & \ddots & 0 & \vdots \\ 0 & 0 & H_{N_L}^L & W_{N_L} \\ W_1^\dagger & \cdots & W_{N_L}^\dagger & H^0 \end{pmatrix}, \qquad (12)$$

where H_λ^L represents the Hamiltonian of lead λ, the Hamiltonian H^0 corresponds to the device region, and W_λ is the coupling between the device and this lead ($\lambda=1,\dots,N_L$). H^0 is composed of the single-particle Hamiltonians H_1 and H_2, corresponding to particles 1 and 2, respectively, and the interaction term V_{12},

$$H^0 = H_1 + H_2 + V_{12}. \qquad (13)$$

The leads (acting as reservoirs) are semi-infinite and therefore, the total Hamiltonian H_{tot} is infinite dimensional. This infinite-dimensional Hamiltonian can be reduced to a non-Hermitian finite-dimensional Hamiltonian $H=H^0+\Sigma$ that describes the *open device* exactly.[36] In this formulation, the influence of the leads is included through a finite-dimensional operator $\Sigma=\Sigma_1+\cdots+\Sigma_{N_L}$. This is the sum of the complex contact self-energies Σ_λ that are nonzero only in the *contact regions* where the lead λ adjoins to the device. The self-energies couple only particle 1 to the leads since particle 2 is assumed to be bound. The Hermitian Hamiltonian H^0 represents the *decoupled device*, i.e., the device with no coupling to the leads. H_1 as well as H_2 are Hamiltonians of the closed device. In the ballistic case, all observables of interest such as transmission functions and the current can be calculated from the retarded Green's function G^R of the open device. This is defined by

$$G^R = (E-H)^{-1} = (E - H_1 - H_2 - V_{12} - \Sigma)^{-1}. \qquad (14)$$

The retarded Green's function can be obtained from the Green's function G^0 of the decoupled device by the Dyson equation

$$G^R = (1 - G^0\Sigma)^{-1}G^0, \qquad (15)$$

which, in turn, can be evaluated from its spectral representation

$$G^0 = \sum_n \frac{|n\rangle\langle n|}{E - \varepsilon_n + i\eta}, \quad \eta \to 0^+, \qquad (16)$$

$$H^0|n\rangle = \varepsilon_n|n\rangle. \tag{17}$$

The direct evaluation of G^R according to Eq. (15) requires the inversion of a huge matrix that is proportional to the number of grid points N_D of the device. By contrast, the CBR method allows one to drastically reduce this effort by utilizing the following exact properties of G^R that remain valid in the present many-particle case. We decompose G^R into four blocks,

$$G^R = \begin{pmatrix} G_C^R & G_{CD}^R \\ G_{DC}^R & G_D^R \end{pmatrix}, \tag{18}$$

where G_C^R is a matrix proportional to the number N_C of contact grid points and is called the *contact block*. Note that $N_C \ll N_D$. For the contact block G_C^R, the following equation holds:

$$G_C^R = (1_C - G_C^0 \Sigma_C)^{-1} G_C^0, \tag{19}$$

where 1_C, G_C^0, and Σ_C are the corresponding contact blocks of the unity matrix G^0 and Σ, respectively. The key point is that this is a linear matrix equation of the order of N_C, since Σ is nonzero only in the contact region. As a consequence, this contact block is also sufficient to determine the transmission functions through the device. The ballistic current can then be calculated from the transmission functions according to the Landauer-Büttiker formalism.[37] In the following, we represent G_C^R in the mixed basis of position eigenstates of particle 1 and energy eigenstates of particle 2,

$$G_C^R(\mathbf{x}_i, \mathbf{x}_j, Y, Z) = \sum_{\alpha_i, \alpha_j} \langle \mathbf{x}_i | \alpha_i \rangle \langle \alpha_i Y | G_C^R | \alpha_j Z \rangle \langle \alpha_j | \mathbf{x}_j \rangle. \tag{20}$$

In this form, G_C^R represents the probability amplitude for the propagation of particle 1 from position $\mathbf{x}_j$ to position $\mathbf{x}_i$, accompanied by a transition of particle 2 from eigenstate $|Z\rangle$ to $|Y\rangle$. For $\lambda \neq \lambda'$, the expression

$$T_{\lambda\lambda'}^{Y,Z}(E) = \text{Tr}_1 \, \Gamma_C^\lambda (G_C^R) \Gamma_C^{\lambda'} (G_C^{R\dagger}), \tag{21}$$

$$\Gamma_C^\lambda = i(\Sigma_C^\lambda - \Sigma_C^{\lambda\dagger}) \tag{22}$$

therefore yields the probability for the transmission of particle 1 from lead λ' to lead λ under the condition that initially particle 2 is in state $|Z\rangle$ and ends up in state $|Y\rangle$. Note that the trace in Eq. (21) is taken only with respect to the position variables of particle 1. If the final state of particle 2 is not measured, the corresponding transmission probability is obtained by summing over all final states of particle 2,

$$T_{\lambda\lambda'}^Z = \sum_Y T_{\lambda\lambda'}^{Y,Z}. \tag{23}$$

In our concrete calculations (see Sec. V), we found it most efficient to first determine the eigenstates of the single-particle Hamiltonians H_1 and H_2 and then diagonalize the interaction V_{12} in the product basis of these single-particle eigenstates. This procedure allows us to take advantage of another built-in efficiency of the CBR method, namely, the fact that only energetically low lying eigenstates of the closed device couple to the incoming and outgoing lead states.[33,34] Consequently, it suffices to take into account only

a reduced set of eigenstates of the single-particle Hamiltonians H_1 and H_2 without affecting the transmission results noticeably.

Another quantity that can be readily obtained from the retarded Green's function G^R is the charge density of the current-carrying states of particle 1. This requires one to know not only the contact block G_C^R but also the submatrix G_{DC}^R. However, the calculation of the submatrix G_{DC}^R only requires one to evaluate the inverse of the small matrix $1_C - \Sigma_C G_C^0$,

$$G_{DC}^R = G_{DC}^0 (1_C - G_C^0 \Sigma_C)^{-1}, \tag{24}$$

where the matrix G_{DC}^0 corresponds to G_{DC}^R in the open device.[34] According to Eq. (20), the latter Green's function reads, in the mixed basis,

$$G_{DC}^R(\mathbf{x}_i, \mathbf{x}_j, Y, Z) = \sum_{\alpha_i, \alpha_j} \langle \mathbf{x}_i | \alpha_i \rangle \langle \alpha_i Y | G_{DC}^R | \alpha_j Z \rangle \langle \alpha_j | \mathbf{x}_j \rangle. \tag{25}$$

The total charge density of the current-carrying states of particle 1 is consequently given by

$$n(\mathbf{x}_j) = \sum_Z n^Z(\mathbf{x}_j), \tag{26}$$

where the contribution

$$n^Z(\mathbf{x}_j) = \frac{1}{2\pi} \sum_\lambda \sum_Y \int dE \, \Xi_\lambda^{Y,Z}(E) f\left(\frac{E - E_F^\lambda}{k_B T}\right), \tag{27}$$

$$\Xi_\lambda^{Y,Z}(E) = \sum_{\mathbf{x}_j} G_{DC}^R(\mathbf{x}_i, \mathbf{x}_j, Y, Z) \Gamma_C^\lambda(\mathbf{x}_j, \mathbf{x}_j) [G_{DC}^R(\mathbf{x}_i, \mathbf{x}_j, Y, Z)]^\dagger \tag{28}$$

results from the projection of the total charge density onto the eigenstate $|Z\rangle$ of the second particle. Here, E_F^λ denotes the Fermi level in lead λ.

III. NUMERICAL DETAILS

A. Electronic structure of particle 1

Equations (1) and (2) are coupled partial differential equations in position space that we discretize and map onto a nonuniform tensor product grid. For the discretization of the all-electric Mach-Zehnder interferometer, a total of 6×10^6 grid points have been used. We employ box integration finite differences in order to ensure flux conservation across boundaries with different material parameters. For the solution of the nonlinear system that results from the discretization of the nonlinear Poisson equation [Eq. (2)], Newton's method with inexact line search is invoked. This remaps the problem into a sequence of linear solutions. We use the Dupont-Kendall-Rachford preconditioned conjugate gradient method for the solution of the resulting linear systems.[38,39] The discretization of the Schrödinger equation [Eq. (1)] results in a large matrix eigenvalue system. However, since the occupation of electron states falls off exponentially with increasing energy distance from the Fermi level, only about

250 quantum states suffice for a converged calculation of the electron density. This allows for the use of the iterative Arnoldi method that is implemented in the published ARPACK libraries.[40] We found that the calculation of eigenvalues and eigenstates can be accelerated by an order of magnitude by invoking a Chebyshev polynomial based spectral transformation that provides an efficient preconditioning of the linear system.[41] Finally, in order to solve the coupled Poisson-Schrödinger system, we employ an approximate quantum charge density inside of Poisson's equation in order to estimate the dependence of the density on the potential through Schrödinger's equation. This corrector-predictor scheme reduces the number of required diagonalizations and accelerates the convergence of the coupled system significantly.[42]

Equation (2) requires the specification of boundary conditions in order to obtain unique solutions. For the potential in the Poisson equation, we generally use von Neumann boundary conditions. Dirichlet boundary conditions are employed at Schottky contacts and at the GaAs/air interfaces. In the former case, the electrostatic potential at the boundary is set equal to the Schottky barrier height, i.e., the difference between the conduction band edge and the quasi-Fermi level. At the GaAs/air interface, on the other hand, the electrostatic potential is determined by the experimentally known Fermi level pinning. The Schrödinger equation for the open quantum system is solved in terms of the CBR method that has been described in detail elsewhere.[34] For the calculation of the transmission probabilities, we have taken into account the lowest 250 eigenstates for the determination of the retarded Green's function of the closed device and the lowest five propagating modes in each of the four leads. The self-consistent solution of Eqs. (1) and (2), for given split gates voltages, takes approximately two days on state-of-the-art personal computer hardware. Converged self-consistent results require typically 12 iterations in the two sets of equations.

B. Entangled Mach-Zehnder double quantum dot device

Our method for the calculation of the ballistic transport properties through a system of two interacting particles requires the diagonalization of the two-particle Hamiltonian including the interaction. This has to be done once for every bias point in the *I-V* characteristics. The diagonalization is performed in the set of product states formed by subsets of the single-particle eigenstates of the two noninteracting particles. We found that a subset of 100 lowest eigenstates of particle 1 is sufficient to obtain convergent transmission functions in the meV energy range around the Fermi level that is relevant for this device.

IV. ANALYTICAL MODEL OF THE TWO-QUBIT DEVICE

Before presenting and discussing the numerical results, we develop a simple analytical model of our two-qubit Mach-Zehnder double-dot system in the present section. The device is shown schematically in Fig. 1. The purpose of this procedure is to be able to better grasp the physics behind the generation of entanglement before we present the numerical
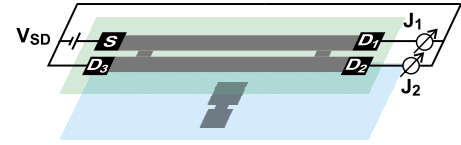

FIG. 1. (Color online) Schematic view of the proposed quantum transport device. The device is realized by two stacked GaAs/AlGaAs 2DEGs. The top 2DEG (green) is depleted by external gates to form a double-QWR based Mach-Zehnder interferometer. The bottom 2DEG (blue) contains two electrostatically defined, coupled quantum dots. The larger one is centered beneath and in between the QWRs. There is a bias voltage V_{SD} applied between the source (S) and the three drain contacts ($D_1 - D_3$) that leads to currents (J_1, J_2) that are labeled accordingly. There are additional gates acting on the device that are shown in Fig. 2. For sake of clarity, the figure is not drawn to scale.

results of the fully three-dimensional self-consistent calculations in the next section.

The good agreement between the two approaches will be a further confirmation of the correct functioning of the device: The results that we obtain for the entangled Mach-Zehnder double quantum dot device are indeed the result of a two-qubit quantum operation. Obviously, the results of the two methods will only be in qualitative agreement with one another, since the analytical model developed in the this section cannot account for the full complexity of the realistic device.

We describe the device consisting of a Mach-Zehnder interferometer coupled to a double quantum dot by two coupled qubits W and D, respectively. The basis states $|0\rangle^W$ and $|1\rangle^W$ of qubit W are defined by an electron that propagates through either of the two QWRs. The basis states $|0\rangle^D$ and $|1\rangle^D$ of qubit D, on the other hand, are defined by the ground states of the isolated quantum dots. Quantum gates can be described by unitary operators that map an initial state $|\Phi_{in}\rangle$ onto a corresponding final state $|\Phi_{fi}\rangle$. The unitary operator $\hat{T}$ that represents our two-qubit quantum transport device can be decomposed into a sequence of unitary operators of less complex single- and two-qubit gates as follows:[22]

$$\hat{T} = \hat{R} \cdot \hat{P} \cdot \hat{V} \cdot \hat{R}. \tag{29}$$

The operators $\hat{R}$ and $\hat{P}$ represent single-qubit gates that act solely on qubit W. In particular, $\hat{R}$ represents a $\pi/2$ rotation gate and describes a coupling window, whereas $\hat{P}$ represents a phase gate that adds a phase difference to the two components of the qubit. The latter can be realized through an additional split gate located on one of the QWRs, as explained in Sec. V. The sequence $\hat{R} \cdot \hat{P} \cdot \hat{R}$ therefore corresponds to a Mach-Zehnder interferometer. The operator $\hat{V}$ represents a two-qubit gate and describes the coupling of the two qubits D and W due to their interaction. This decomposition allows us to specify the action of the single-qubit gates $\hat{R}$ and $\hat{P}$ directly in terms of unitary operators.

We proceed by describing the entangled Mach-Zehnder double-dot device as a stationary quantum-mechanical scat-

tering problem. To this end, we represent the two electrons in the pair of QWRs and the double quantum dot by the following eight basis states for a given total energy E and a given position x,

$$\psi_{\pm k_J, \sigma J}(x) = \exp(\pm i k_J x)|\sigma\rangle^{\mathrm{W}}|J\rangle^{\mathrm{D}} \quad (\sigma, J = 0, 1). \quad (30)$$

These states describe the two electrons as follows: The first electron propagates along the wire axis x in either of the two states $|0\rangle^{\mathrm{W}}$ and $|1\rangle^{\mathrm{W}}$, corresponding to the two QWRs. The electron momentum at position x is denoted by k_J. The second electron occupies one of the two quantum dots, represented by states $|0\rangle^{\mathrm{D}}$ and $|1\rangle^{\mathrm{D}}$. In this representation, the operators in Eq. (29) correspond to 8×8 transfer matrices,

$$T = T_{\hat{R}} \cdot T_{\hat{P}} \cdot T_{\hat{V}} \cdot T_{\hat{R}}. \quad (31)$$

This will allow us to finally determine the transmission function through the device. As a first step, we derive the transfer matrix $T_{\hat{V}}$ of the two-qubit gate $\hat{V}$ by solving a two-particle Schrödinger equation. The noninteracting two-particle Hamiltonian that describes the dynamics of the system is given by

$$H_0 = \frac{p_x^2}{2m} + H_2. \quad (32)$$

Here, H_2 is the model Hamiltonian that describes a pair of tunneling-coupled quantum dots in terms of the bare splitting Δ and the tunneling coupling t in accordance with Eq. (6). For the Coulomb interaction between the two electrons, we make the following ansatz:

$$V(x) = U|1\rangle^{\mathrm{W}}|1\rangle^{\mathrm{D}}\langle 1|^{\mathrm{W}}\langle 1|^{\mathrm{D}} \theta(x) \theta(L - x). \quad (33)$$

This describes a localized interaction with interaction strength U that is nonzero only for the two-particle state $|1\rangle^{\mathrm{W}}|1\rangle^{\mathrm{D}}$ but zero for all other states. In addition, the interaction vanishes if the position of the QWR electron lies outside the spatial interval from $x=0$ to $x=L$. The resulting quantum-mechanical scattering problem,

$$H = H_0 + V(x), \quad (34)$$

can be solved analytically for the 8×8 transfer matrix $T_{\hat{V}}(E)$. Since $V(x)$ only acts on the state $|1\rangle^{\mathrm{W}}|1\rangle^{\mathrm{D}}$, $T_{\hat{V}}$ has the following form:

$$T_{\hat{V}} = \begin{pmatrix} \mathbf{1}_{4 \times 4} & 0 \\ 0 & \tau \end{pmatrix}, \quad (35)$$

where τ is a 4×4 submatrix that connects the states $\sigma = 1$, i.e., states that contain $|1\rangle^{\mathrm{W}}$. In order to determine this submatrix, we split the x axis into three regions $x < 0$, $0 < x < L$, and $x > L$. Within each region, the Hamiltonian H can be diagonalized. Requiring continuity and differentiability, we obtain the following explicit expression for the submatrix τ. In this expression, we have transformed the basis by using the bonding and antibonding dot states $|A\rangle^{\mathrm{D}}$ and $|B\rangle^{\mathrm{D}}$ from Eqs. (7) and (8) instead of the states $|0\rangle^{\mathrm{D}}$ and $|1\rangle^{\mathrm{D}}$. In this basis, we obtain $\tau = \kappa_L^{-1} \mu_L \kappa_0^{-1} \mu_0$, where the submatrices μ and κ and read, for $x_1 = 0$ and $x_2 = L$,

$$\mu_{x_i} = \begin{pmatrix} \nu_{x_i}(k_B) & 0 \\ 0 & \nu_{x_i}(k_A) \end{pmatrix}, \quad (36)$$

$$\kappa_{x_i} = \begin{pmatrix} \alpha_B \nu_{x_i}(q_B) & \alpha_A \nu_{x_i}(q_A) \\ \beta_B \nu_{x_i}(q_B) & \beta_A \nu_{x_i}(q_A) \end{pmatrix}, \quad (37)$$

where $i = 1, 2$. The 2×2 matrix $\nu_{x_i}(k)$ is defined as follows:

$$\nu_{x_i}(k) = \begin{pmatrix} \exp(ikx_i) & \exp(-ikx_i) \\ ik \exp(ikx_i) & -ik \exp(-ikx_i) \end{pmatrix}. \quad (38)$$

The coefficients α_Y and β_Y and the wave vectors k_Y and q_Y $(Y = A, B)$ are given by $(t, U > 0)$

$$\alpha_Y = \frac{tU}{\sqrt{[4E_Y(E_Y + \varepsilon) + \Delta U]^2 + t^2 U^2}}, \quad (39)$$

$$\beta_Y = \frac{4E_Y(E_Y + \varepsilon) + \Delta U}{\sqrt{[4E_Y(E_Y + \varepsilon) + \Delta U]^2 + t^2 U^2}}. \quad (40)$$

$$k_Y = \frac{1}{\hbar}\sqrt{2m(E - E_Y)}, \quad (41)$$

$$q_Y = \frac{1}{\hbar}\sqrt{2m\left(E - \frac{1}{2}U \mp \varepsilon\right)}, \quad (42)$$

where $\varepsilon = \frac{1}{2}\sqrt{t^2 + (U + \Delta)^2}$. Note that the electron wave vectors k_Y arise from the region $x < 0$ and from $x > L$, whereas q_Y arises from the central region.

The next step is to determine the transfer matrices $T_{\hat{R}}$ and $T_{\hat{P}}$ from the following representations of ideal rotation and phase gates:

$$\hat{R} = \begin{pmatrix} \cos(\theta/2) & -\sin(\theta/2) \\ \sin(\theta/2) & \cos(\theta/2) \end{pmatrix}, \quad \theta = \pi/2, \quad (43)$$

$$\hat{P} = \begin{pmatrix} e^{i\phi/2} & 0 \\ 0 & e^{-i\phi/2} \end{pmatrix}, \quad (44)$$

where ϕ is the phase gate angle. We assume that these gates do not introduce backscattering. In this case, we can apply $\hat{R}$ and $\hat{P}$ separately for both directions of propagation. This leads to unitary matrices $T_{\hat{R}}$ and $T_{\hat{P}}$ with the following nonvanishing elements:

$$(T_{\hat{R}})_{j,j} = \cos(\theta/2), \quad (T_{\hat{R}})_{i,i+4} = (-1)^i \sin(\theta/2), \quad (45)$$

$$(T_{\hat{R}})_{i+4,i} = (-1)^{i+1} \sin(\theta/2), \quad (i = 1, 4; j = 1, 8) \quad (46)$$

$$(T_{\hat{P}})_{j,j} = \exp\left[(-1)^{j+1}\frac{\phi}{2}\right] \quad (j = 1, 8). \quad (47)$$

This completes the calculation of the total transfer matrix T. The final step is to determine the transmission function which requires us to set an initial condition for the scattering problem. We consider the situation where the propagating electron enters the pair of QWRs from the left in state $|0\rangle^{\mathrm{W}}$.

We further assume that the electron in the double quantum dot lies initially in the binding state $|B\rangle^{\mathrm{D}}$. The eight final state coefficients represent the transmission amplitudes into the four states $|\sigma\rangle^{\mathrm{W}}|Y\rangle^{\mathrm{D}}$ ($\sigma=0,1$, $Y=A,B$) for each of the two asymptotic propagation directions (to the right or to the left). We denote these final state coefficients by $E^r_{\sigma,Y}$ and $E^l_{\sigma,Y}$, respectively. By construction, the two rotation gates and the phase gate do not introduce any backscattering. The amount of backscattering due to the interaction $V(x)$ depends on the ratio of the interaction strength U and the length L of the interaction region and can be made arbitrarily small. Thus, the transmission amplitudes $E^l_{\sigma,Y}$ are negligible. In addition, we only need the transmission probabilities T_1 and T_2 that describe the total probability of an electron to arrive at $|0\rangle^{\mathrm{W}}$ or $|1\rangle^{\mathrm{W}}$, irrespective of the state of the double-dot electron,

$$T_1 = \left|E^r_{0,A}\right|^2 + \left|E^r_{0,B}\right|^2, \tag{48}$$

$$T_2 = \left|E^r_{1,A}\right|^2 + \left|E^r_{1,B}\right|^2. \tag{49}$$

The resulting transmission probabilities T_1 and T_2 will be presented in the following section for different values of the tunneling coupling. They will be compared with the numerical results obtained with the realistic model described in Sec. II. Indeed, the above comparison will show that the two models are able to reproduce the basic physics of the device and that the device is able to produce an entangled state of the two qubits.

V. RESULTS AND DISCUSSION

The method presented in the Sec. II allows us to calculate the ballistic current through entangled two-particle systems. Concretely, we first present results for a double-QWR based Mach-Zehnder interferometer and show that this interferometer can be employed as a fully controllable single-qubit gate. Based on this system, we then propose a two-qubit quantum transport device that allows the controlled generation and measurement of entanglement between the QWR qubit and the double quantum dot qubit. The measurement involves only the dc I-V characteristics, and no higher order current correlations or magnetic fields are required to detect entanglement. We would like to emphasize that the subject of this paper is to show that these devices are well suited to prepare arbitrary single-qubit and entangled two-qubit states. Actual quantum computing applications, however, require additionally the performance of these operations in a time-resolved fashion with single electrons.

A schematic view of the proposed two-qubit device is shown in Fig. 1. It is based on a GaAs/AlGaAs heterostructure that consists of two vertically stacked 2DEGs. The 2DEGs are locally depleted by the application of negative voltages to appropriate metal top and bottom gates that are not shown in this figure. For suitable gate voltages, the top gates create a pair of parallel QWRs in the upper 2DEG that are connected to each other by two coupling windows. For specific energies, these coupling windows act as beam splitters and the QWR network behaves as an electronic Mach-Zehnder interferometer. In contrast to electronic Mach-
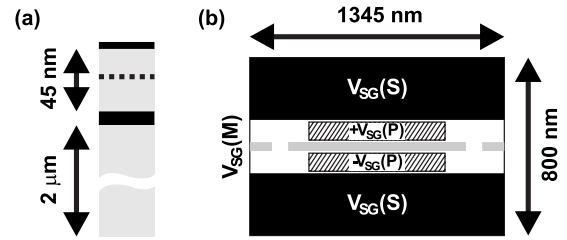

FIG. 2. (a) Vertical cross section of the GaAs/AlGaAs heterostructure with a single 10 nm wide GaAs quantum well that is used for the Mach-Zehnder interferometer. GaAs is shown in black; $\mathrm{Al_{0.37}Ga_{0.63}As}$ is shown in gray. The GaAs cap layer is 5 nm thick. A silicon δ doping layer with a concentration of 2.5×10^{12} cm^{-2} is located 25 nm below the surface (dashed line). (b) Top view of the Mach-Zehnder interferometer that depicts the side gates (black) with voltage $V_{\mathrm{SG}}(\mathrm{S})$ and the mid gates (gray) with voltage $V_{\mathrm{SG}}(\mathrm{M})$ that define the two QWRs and the coupling windows between them. On top of the wires, there are two additional phase gates (hatched) at a bias of $\pm V_{\mathrm{SG}}(\mathrm{P})$.

Zehnder interferometers based on quantum Hall edge channels,[32] no magnetic fields are employed. We therefore use the term *all-electric Mach-Zehnder interferometer* for this kind of device. We note that the relative phase shift between the electronic wave function in the two QWRs is controlled electrostatically by phase gates. These are additional top gates but may be combined with the gates that are used to define the QWRs in the first place. The lower 2DEG contains the two electrostatically defined tunneling-coupled single-electron quantum dots. An electron in the upper 2DEG couples to the electron in the double quantum dot in the lower 2DEG by means of the Coulomb interaction. We have designed the entire device so that the consequences of entanglement become markedly evident in the observables, and we refer to it as *entangled Mach-Zehnder double quantum dot device*.

The Mach-Zehnder interferometer is operated under ballistic transport conditions. By applying a small dc bias voltage V_{SD} between the upper left source S and the remaining three drain contacts D_1, D_2, and D_3, the device can be used in such a way that current flows predominantly from S to D_1 (denoted by J_1) or to D_2 (denoted by J_2), as indicated in Fig. 1.

A. Results: All-electric Mach-Zehnder interferometer (single-qubit device)

First, we turn to the I-V characteristics of the single-electron device, i.e., the all-electric Mach-Zehnder interferometer alone. The calculations have been based on the GaAs/AlGaAs heterostructure that is depicted schematically in Fig. 2. It consists of a 5 nm thick GaAs cap layer [see vertical cross section in Fig. 2(a)], followed by a 45 nm barrier of $\mathrm{Al_{0.37}Ga_{0.63}As}$ and a 10 nm GaAs 2DEG layer. Beneath, there lies a 2 μm $\mathrm{Al_{0.37}Ga_{0.63}As}$ substrate. A silicon δ doping layer with a concentration of 2.5×10^{12} cm^{-2} is located 25 nm below the surface. The electron sheet density in the 2DEG layer has been calculated to be 2.4×10^{11} cm^{-2} for the ungated sample at a temperature of 4 K.
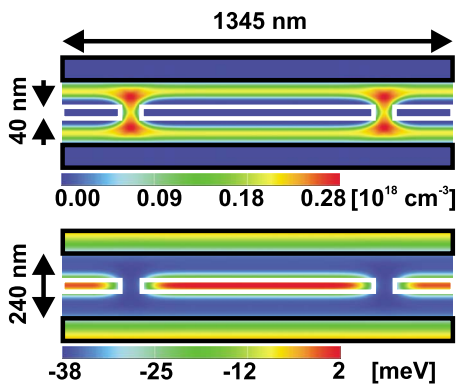
FIG. 3. (Color online) Top views of the equilibrium electron density (upper panel) and electrostatic potential (lower panel) within the upper 2DEG. The black and the white frames indicate the position of the metal side and mid gates.

Figure 2(b) shows a top view of the structure including the gates. The source and drain contacts (cf. Fig. 1) are not shown in this figure. The device is 800 nm wide and 1345 nm long. Here, we distinguish three types of gates: side gates (black), mid gates (gray), and phase gates (hatched). Each of the two side gates is, respectively, 280 nm wide, 1345 nm long, and biased at $V_{SG}(S)=-0.245$ V with respect to the source. The three mid gates are 40 nm wide and 200, 800, and 200 nm long, respectively. We apply a gate voltage of $V_{SG}(M)=-0.660$ V to the mid gates. They define two QWRs (white) with a nominal width of 100 nm as well as two coupling windows, each with a nominal length of 72.5 nm in the direction parallel to the wires. All of these structural parameters have been chosen to guarantee optimal device operation while allowing for its fabrication with current technologies.

The subband spacing of the two lowest subbands in each of these QWRs amounts to 3.1 meV. It is important for the interferometer that the Fermi wavelength is close to the length of the coupling windows. Indeed, our calculations yield a Fermi wavelength of $\lambda_F=77$ nm in the lowest subband. In order to control the relative phase of the electron wave function in the two QWRs, small gate voltages of $+V_{SG}(P)$ and $-V_{SG}(P)$ are applied to the phase gates, respectively. The two phase gates are centered on top of the two QWRs and are each 720 nm long and 95 nm wide. A separating layer of resist could be used to reliably insulate the phase gates from the other gates. Figure 3 shows the equilibrium charge density (upper panel) and the corresponding potential (lower panel) in the 2DEG layer of the Mach-Zehnder interferometer. The black and the white framed rectangles indicate the position of the metal top gates. The upper panel shows the 2DEG to be fully depleted underneath the gates. In addition, it is evident from the figure that the QWRs and the coupling windows are formed indeed. The wires are strictly one dimensional in the sense that only the lowest subband contributes to the density. The lower panel shows the potential barrier that separates the two QWRs. The energy scale is chosen so that the Fermi level lies at 0 meV.

Figure 4(a) shows the currents J_1 (solid), J_2 (dashed), as well as the backscattered current J_3 (dotted) that flow from
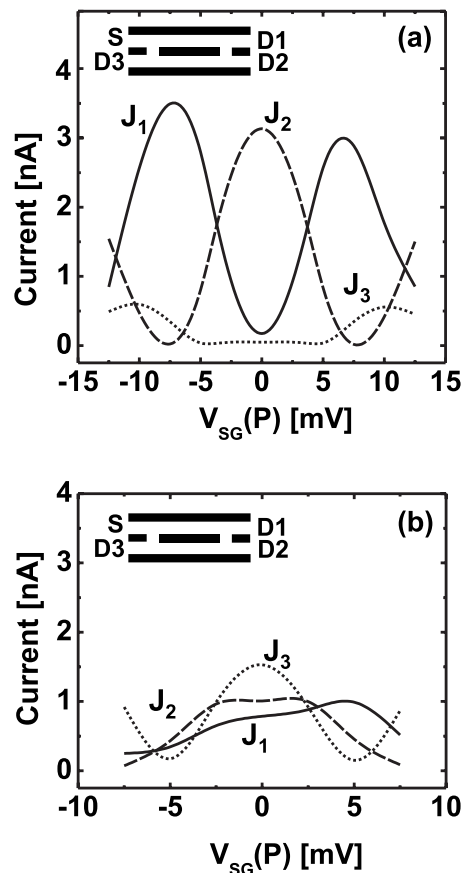

FIG. 4. (a) Stationary currents J_1 (solid), J_2 (dashed), and J_3 (dotted) through the Mach-Zehnder interferometer as a function of the phase gate voltage $V_{SG}(P)$ for a nominal length of the coupling windows of 72.5 nm. The source-drain voltage V_{SD} is set to 50 μV. (b) Same as (a), but for a coupling window length of 67.5 nm.

the source S to D_1, D_2, and D_3, respectively. The currents have been calculated by assuming a dc bias voltage of 50 μV and a temperature of 30 mK. The figure shows the dependence of the currents on the voltages $+V_{SG}(P)$ and $-V_{SG}(P)$ applied to the two phase gates, respectively. We first note that the back current J_3 is smaller than 0.5 nA for the entire relevant range of gate voltages and is therefore negligible. In contrast to J_3, the currents J_1 and J_2 strongly depend on the gate voltage and oscillate between 0 and 4 nA for more than 1.5 oscillation periods. The currents J_1 and J_2 are seen to be phase shifted relative to one another by 180°, which confirms that the device actually behaves as a Mach-Zehnder interferometer. Note that this Mach-Zehnder interference pattern becomes damped out once the absolute gate voltage $|V_{SG}(P)|$ exceeds 15 mV because this increases the amount of backscattering. Backscattering can be suppressed, however, by increasing the length of the device, because the phase shift depends linearly on the length of the phase gate, whereas backscattering is independent of the length but increases with the magnitude of $|V_{SG}(P)|$.

For comparison, Fig. 4(b) depicts the calculated currents J_1, J_2, and J_3 for the same device but for a nominal length of the coupling windows that has been reduced by 5 nm. The difference in results shows the sensitivity of the interference
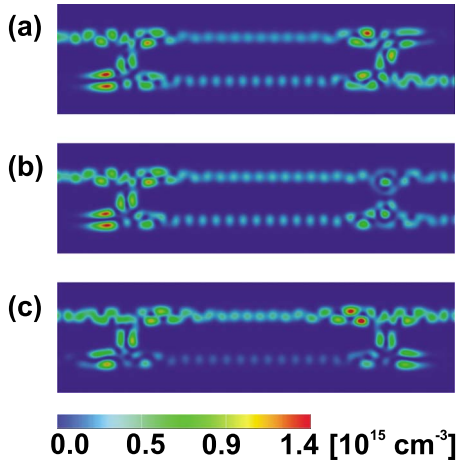
FIG. 5. (Color online) Charge densities associated with the current-carrying scattering states for a phase gate voltage $V_{SG}(P)$ of (a) 0 meV, (b) −3.6 meV, and (c) −7.5 meV. In all cases, the source-drain voltage V_{SD} is set to 50 μV.

pattern to small changes in geometry and implies very high demands on fabrication precision.

Figure 5 shows the charge densities of the stationary current-carrying states of the Mach-Zehnder interferometer for selected phase gate voltages. Figures 5(a)–5(c) correspond to gate voltages of $V_{SG}(P)=0$, −3.6, and −7.5 mV, respectively. The three graphs show that the quantum-mechanical charge densities change predominantly near the drain contacts on the right hand side of the device. These changes reflect the redistribution of the total current between J_1 and J_2. In Fig. 5(a), the charge density is zero near the upper right terminal but large near the lower right terminal. This agrees with Fig. 4(a) that shows that the current J_1 is minimal (J_2 maximal) for the corresponding gate voltage $V_{SG}(P)=0$ mV. In Fig. 5(b), on the other hand, the charge density is seen to be almost equal near both right drain contacts, again in accord with Fig. 4(a) for $V_{SG}(P)=-3.6$ mV. Finally, the charge density is large near the upper right terminal but zero at the lower right terminal in Fig. 5(c), again in correspondence with Fig. 4(a).

All of these effects are a consequence of the self-interference of the electron wave function. Depending on the relative phase between the two QWRs, the interference at the second beam splitter leads to partial extinction either near the upper or the lower right terminal.

B. Discussion: Switching characteristics of the all-electric Mach-Zehnder interferometer

The dc transfer characteristics shown in Fig. 4(a) exhibit multiple pronounced maxima and minima that can be attributed to rotations of a qubit on the Bloch sphere. Before entering into the discussion of the results, let us give a rigorous definition of the Mach-Zehnder interferometer qubit state. To this aim, we depict the device schematically in Fig. 6, where we show the regions of the two coupling windows and the phase gate that perform the $\hat{R}$ and $\hat{P}$ transformations of Eqs. (43) and (44), respectively. We define the basis states $|0\rangle$ and

FIG. 6. Schematic representation of the Mach-Zehnder interferometer. We have indicated the three quantum-operation regions, consisting of the two coupling windows $\hat{R}$ and one phase gate $\hat{P}$, and four other segments where the qubit state is well defined (see Table I).

$|1\rangle$ of the QWR qubit by an electron scattering state localized in the upper and lower QWRs, respectively. This definition holds only in the regions where the two channels are well separated, as in the segments I, II, III, and IV of Fig. 6. By contrast, the qubit state is not well defined within the window regions $\hat{R}$, where the barrier between the QWRs is very small. As an example, the approximate qubit states for the four regions indicated in Fig. 6 are included in Table I and specified for each of the three cases depicted in Fig. 5. Indeed, in the calculation of Fig. 5, the split gate voltages have been chosen in order to obtain a qubit rotation angle $\theta = \pi/2$ and phase angles $\phi=0, \pi/2, \pi$ in (a), (b), (c), respectively [cf. Eqs. (43) and (44)].

Since it is unlikely that one can fabricate the device discussed in Fig. 2 precisely, it is imperative to understand the dependence of the Mach-Zehnder interferences on the various device geometry parameters such as width and length of the QWRs and the coupling windows not only quantitatively but also qualitatively. A physically transparent picture can be obtained by studying a model H shaped structure that consists of a single coupling window where the depletion potentials are hard-wall potentials as depicted in the inset of Fig. 7.

The coupling between the two QWRs causes the transmission to become resonant for specific energies that depend on the length L and width W of the coupling window. These energies are approximately equal to the energies of the bound states in a rectangular box with the dimensions of the coupling window, i.e.,

$$E(n,m) \propto \frac{n^2}{L^2} + \frac{m^2}{W^2}.$$ (50)

Beam splitting, i.e., a crossover in the transmission from channel S-D_1 to S-D_2, requires that the corresponding trans-

TABLE I. Quantum state of the Mach-Zehnder qubit in the four device segments indicated in Fig. 6 (columns), corresponding to the three situations shown in Fig. 5 (rows), respectively.

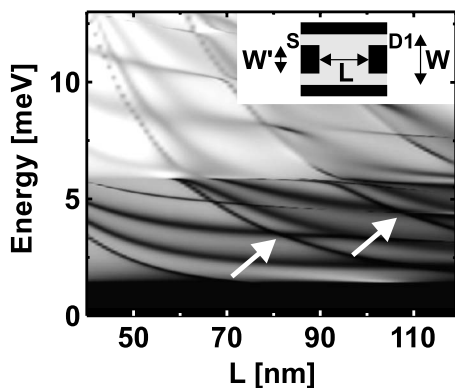| Charge density	Mach-Zehnder interferometer region			
	I	II	III	IV
Figure 5(a)	$\|0\rangle$	$\|0\rangle+\|1\rangle$	$\|0\rangle+\|1\rangle$	$\|1\rangle$
Figure 5(b)	$\|0\rangle$	$\|0\rangle+\|1\rangle$	$(1+i)\|0\rangle+(1-i)\|1\rangle$	$i\|0\rangle+\|1\rangle$
Figure 5(c)	$\|0\rangle$	$\|0\rangle+\|1\rangle$	$i\|0\rangle-i\|1\rangle$	$i\|0\rangle$

FIG. 7. Contour plot of the transmission function T_1 between source S and drain D_1 as a function of kinetic energy in meV and as a function of the coupling window length L in nm. The total width of the structure equals $W=220$ nm, whereas the width of the inner coupling windows amounts to $W'=100$ nm. The darker the color, the smaller the value of T_1. The dark lines therefore indicate minima in T_1. The arrows point to crossings of resonances where T_1 vanishes.

mission functions obey the relation $T_1(E_0) \approx T_2(E_0) \approx 0.5$ for some energy E_0. In turn, this condition requires that there are two sets of values (n,m) that correspond to the same energy E, i.e., $E(n_1,m_1)=E(n_2,m_2)$. Thus, the crucial geometric requirement for quantum-mechanical switching is to achieve an appropriate ratio of length L and width W that obeys this condition. In order to obtain a pronounced resonance, the values of n and m should be of the order of unity additionally, since the resonances lie densely in energy for large integers. Figure 7 shows a contour graph of the transmission probability T_1 (from source S to drain D_1) as a function of the coupling window length L and the kinetic energy of the electron. The arrows in this figure point to suitable values of the length L where the energies of two eigenstates cross. To further illustrate this crossover in the transmissions, Fig. 8 shows a cross section through Fig. 7 for the length L $=82$ nm that is marked by the leftmost white arrow. This crossing corresponds to the switching from channel S-D_1 to
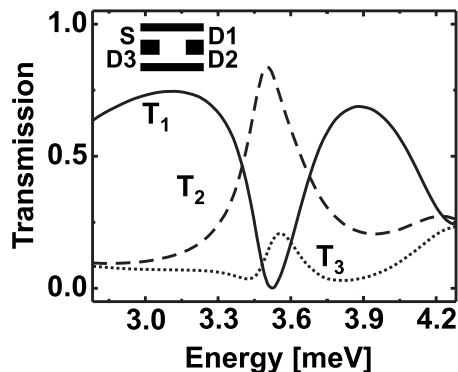

FIG. 8. Transmission functions T_1 (solid), T_2 (dashed), and T_3 (dotted), as a function of the kinetic energy of the electron in meV. The length L of the coupling window has been set equal to 82 nm. The other symbols have been defined in Fig. 1.

S-D_2 and occurs near the degeneracy of the energy states $E(1,3)$ and $E(2,1)$.

C. Results: Entangled Mach-Zehnder double quantum dot device (two-qubit device)

In the following, we present the results for the entangled Mach-Zehnder double quantum dot device that has been schematically depicted in Fig. 1. For these calculations, we have used a somewhat different set of geometry parameters for the Mach-Zehnder interferometer in order to optimize the entanglement. Since the calculations of the entangled system are very demanding, we have defined the Mach-Zehnder interferometer by a hard-wall potential within a 10 nm thick slab of GaAs rather than performing a charge-self-consistent calculation including all metal gates. We have taken the two QWRs to be 55 nm wide and 1000 nm long, and the lateral distance between them has been set to 20 nm. The coupling windows now have a length of 85 nm. The resulting energy spacing of the two lowest subbands amounts to 5.3 meV, which is nearly twice as large as in the Mach-Zehnder device of Sec. V A. The Fermi level E_F has been set to 1.6 meV in the lowest subband. This Fermi level causes the two coupling windows to act as almost perfect beam splitters, with channel transmissions $T_1(E_F) \approx T_2(E_F) \approx 0.5$. For the calculation of the interaction between the Mach-Zehnder interferometer and the double quantum dot, we assume a vertical distance of 80 nm between them. The larger of the two quantum dots with a lower ground state energy is located exactly underneath the center of the Mach-Zehnder interferometer, whereas the smaller one lies 60 nm away in the direction perpendicular to the QWRs. The double quantum dot system is modeled by the Hamiltonian given in Eq. (6). The positions of the Mach-Zehnder interferometer and the double quantum dot relative to each other have a large influence on the operation characteristics of the device. The present configuration exploits the idea that the interaction between the electron in the QWRs and the electron in the larger quantum dot is identical for both wires. The electron in the smaller quantum dot, on the other hand, lies closer to the QWR between gates D_2 and D_3 and interacts mostly with the electron in that wire. Consequently, a phase difference in the electron wave function for the two QWRs is exclusively induced by the electron in the smaller dot.

At first, we study the transfer characteristics of the device for a situation where the tunneling between the quantum dots is inhibited ($t=0$). The ground states of the larger and the smaller quantum dot are assumed to differ by $\Delta=10$ μeV. The resulting current in the QWRs is shown in Fig. 9 by the dashed curves. We obtain the typical interference pattern that we have also found in Sec. V A for the all-electric Mach-Zehnder interferometer. The asymmetry with respect to the sign of the gate voltage is caused by the asymmetric position of the phase gate along only one of the two QWRs in combination with the additional repulsive potential due to the electron in the double quantum dot.

We now allow the electron in the double quantum dot to tunnel between the two dots ($t=10$ μeV). The currents J_1 and J_2 that correspond to this situation are shown in Fig. 9 by
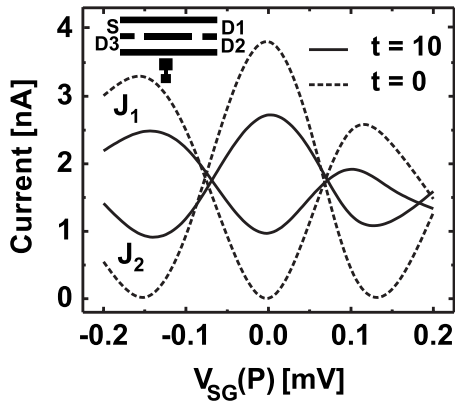
FIG. 9. Currents J_1 and J_2 in nA as a function of the phase gate voltage $V_{SG}(P)$ in mV for two different quantum dot tunneling couplings t in μeV. The inset is a simplified version of Fig. 1.

the solid curves. We still obtain the Mach-Zehnder interference pattern, but the visibility is markedly reduced. Let us define the visibility by

$$v = (J_2 - J_1)/(J_2 + J_1)|_{V_{SG}(P)=0}, \qquad (51)$$

i.e., for zero phase gate voltage $V_{SG}(P)$. Figure 10 shows the visibility as a function of the tunneling coupling. The visibility is almost 1 for vanishing tunneling coupling and decreases monotonously with increasing tunneling. The visibility is therefore uniquely related to the magnitude of the tunneling coupling. The above effect can be explained as follows. If the tunneling probability is high, the double-dot electron can easily change its state. In this regime, it is also easy for the double dot to *measure* the path of the interferometer particle, thus causing decoherence and destroying the interference. For low tunneling probability, on the other hand, the electron that sits initially in the large dot is insensitive to the Coulomb interaction with the interferometer. When the tunneling is completely suppressed, the state of the dot is fixed and the interferometer electron is unable to change the dot state. While the electrons are still interacting
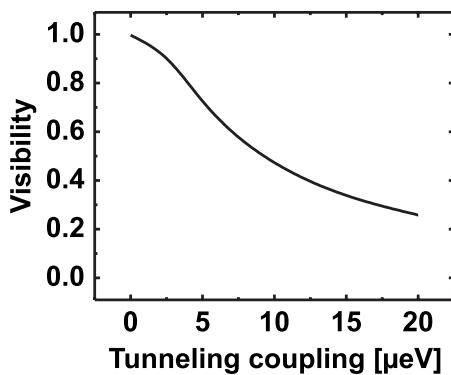

FIG. 10. Visibility as defined in the text, corresponding to the interference pattern of Fig. 9, as a function of the tunneling coupling in μeV.
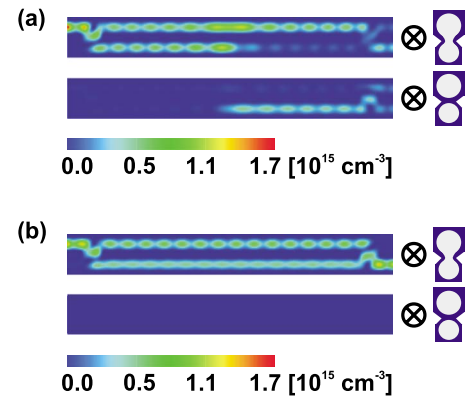

FIG. 11. (Color online) (a) Contour plot of the stationary charge density of the current-carrying states, in units of 10^{15} cm^{-3}. The upper (lower) panel shows the single-particle electron density in the QWRs when the electron in the quantum dot occupies the bonding (antibonding) state. The quantum dot tunneling coupling amounts to $t=10$ μeV. (b) Same type of figure, but with the Coulomb interaction between the electron in the wires and the electron in the quantum dot switched off. In case (b), the two possible paths of the scattered electron can interfere with one another. In case (a), however, the electron propagating in the lower wire changes the double-dot state and loses its capability to interfere with the other path, thus reducing the visibility (see text).

due to their charge in this case, the path of the interferometer particle is not measured by the double dot.

Figures 11(a) and 11(b) show the electron density [Eq. (27)] in the entangled Mach-Zehnder double quantum dot device. To be precise, the figures depict the projection of the probability densities of the current-carrying two-particle states onto the eigenstates of the isolated double quantum dot for a tunneling coupling of $t=10$ μeV and vanishing phase gate voltage $V_{SG}(P)$. In particular, Fig. 11(a) shows the interacting case, whereas Fig. 11(b) shows the noninteracting case where the electron-electron interaction between the electrons in the Mach-Zehnder interferometer and the quantum dot electron has been switched off. Thus, the two figures illustrate the effect of the Coulomb interaction on the charge density. In each of the two figures, the upper panel corresponds to the ground state and the lower panel corresponds to the excited state of the double quantum dot, respectively. In the interacting case (a), we find a finite probability of the electron in the double quantum dot to be in the excited state. This has to be compared to the case of vanishing interaction (b), as well as to the case of zero tunneling coupling. In each of the latter cases, the probability of the electron in the double quantum dot to be in the excited state is zero. This is shown in Fig. 11(b). Note that for cases (a) and (b), the total probability densities that are given by the sum of the two projected probability densities are almost identical near the left contacts but differ significantly near the right contacts. In (a), the total probability density near the upper right contact is only partially extinct by interference, whereas in (b), the total probability density vanishes near the upper right contact. This indicates that the interaction between the Mach-Zehnder interferometer and the double quantum dot destroys the self-interference of the QWR-electron wave function.
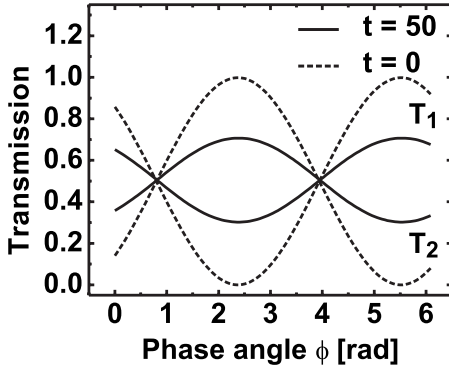
FIG. 12. Transmission functions T_1 and T_2 as a function of the phase angle in rad for the analytical model of the entangled Mach-Zehnder double quantum dot device. The full line is for a finite tunneling coupling $t=50$ in units of $\hbar^2/2mL^2$, whereas the dashed curve is for vanishing tunneling coupling that corresponds to no entanglement.

D. Discussion: Visibility and von Neumann entropy of the entangled Mach-Zehnder double quantum dot device

The results that we have obtained for the entangled Mach-Zehnder double quantum dot device are indeed the result of a two-qubit quantum operation. In order to show this, we apply the analytical model developed in Sec. IV to our two-qubit device. Figure 12 shows the transmission probabilities T_1 and T_2, computed from Eqs. (48) and (49), for two different values of the quantum dot tunneling. Indeed, the comparison with Fig. 9 shows that the model is able to reproduce the basic physics of the device and to yield transmission probabilities T_1 and T_2 that qualitatively agree with the results obtained by the numerical simulations described in Secs. II and III. In particular, Figs. 9 and 12 show a similar dependence of the visibility on the tunneling coupling. The reason for the suppression of the visibility is the entanglement of the two qubits. In fact, from the point of view of the individual qubit, its entanglement with the other one is nothing else but decoherence, and this decoherence partially suppresses the interference of the electron wave function in the two QWRs. In other words, the reduced density matrix of each of the qubits, obtained by tracing out the degrees of freedom of the other qubit, represents a mixed state if and only if the two qubits are entangled. Thus, the observed suppression of the visibility is both a direct measure of the degree of entanglement between two qubits and of the decoherence undergone by the QWR qubit.

We stress that our approach does not include other sources of decoherence as, for example, electron-phonon interaction or charge fluctuations in the metallic split gates that define the structure. Therefore, our reduction of the visibility is obviously ascribed to the quantum entanglement of the two qubits. On the other hand, in real experiments, the visibility will be reduced by the coupling of the interferometer with any external degree of freedom and not only with the other qubit. What makes our results functional to experiments is the estimation of the visibility decrease against tunable parameters of the realistic device, as, for example, the tunneling coupling of the second qubit. In fact, it is unlikely that

the effect of the environment will be tuned by the same parameters that affect the amount of entanglement between the two qubits. The phonon effects on the interferometer, for example, are determined solely by the temperature, the structure composition, and the energy of the traveling electrons. Thus, our proposed device demonstrates—from a modeling perspective—a controlled generation of two-qubit entanglement. The predicted behavior of the visibility against various system parameters may serve as an entanglement witness in experimental realizations of the system.

In the remainder of this section, we show that the relation between the visibility of our device, as defined in Eq. (51) and depicted in Figs. 10 and 12, and the entanglement can be quantified in terms of the von Neumann entropy of the reduced density matrix[7,43] that is a measure of the degree of entanglement.

To simplify the derivation, we generally assume that backscattering is negligible in the directional couplers and phase gates. This reduces all matrices to size 4×4 and allows the analytical evaluation of the transmissions T_1 and T_2 in Eqs. (48) and (49). The density matrix of the final state is then given by

$$\rho = \sum_{\sigma,\sigma'=0,1} \sum_{Y,Y'=A,B} E^r_{\sigma,Y} E^{r*}_{\sigma',Y'} |\sigma\rangle^{\mathrm{W}} |Y\rangle^{\mathrm{D}} \langle\sigma'|^{\mathrm{W}} \langle Y'|^{\mathrm{D}}. \quad (52)$$

The amount of entanglement of the final two-qubit state is given by the von Neumann entropy of the reduced density matrix, namely,

$$S = -\operatorname{Tr} \rho_{\mathrm{red}} \log \rho_{\mathrm{red}}, \quad (53)$$

where the reduced density matrix ρ_{red} is obtained from ρ by tracing out the electron in the double quantum dot. This yields the 2×2 matrix

$$\rho_{\mathrm{red}} = \begin{pmatrix} T_1 & Z \\ Z^* & T_2 \end{pmatrix}, \quad (54)$$

where the so-called coherence Z is given by

$$Z = E^r_{0,A} E^{r*}_{1,A} + E^r_{0,B} E^{r*}_{1,B}. \quad (55)$$

With the eigenvalues of the reduced density matrix,

$$p_\pm = \frac{1}{2}(1 \pm \sqrt{4(|Z|^2 - T_1 T_2) + 1}), \quad (56)$$

the von Neumann entropy reads

$$S = -\sum_{i=+,-} p_i \log p_i. \quad (57)$$

We now show that the eigenvalues $p_\pm$ of ρ_{red} can be expressed in terms of the visibility v, Eq. (51), of the interference pattern according to

$$p_\pm = \frac{1}{2}(1 \pm v). \quad (58)$$

First, we determine the explicit expressions for the transmission functions as a function of the angle ϕ of the phase gate. To this end, we first apply the $\pi/2$ rotation gate $\hat{R}$ and the two-qubit gate $\hat{V}$ onto the initial state $|\Phi_{\mathrm{in}}\rangle$. The probabilities

$|A_{\sigma,Y}|^2$ of the four two-particle basis states $|\sigma\rangle^W|Y\rangle^D$ ($\sigma = 0, 1$, $Y = A, B$) of the resulting state are given by

$$|A_{\sigma,B}|^2 = \frac{1}{2}\cos^2\left(\frac{1}{2}(\beta \pm \gamma)\right),$$

$$|A_{\sigma,A}|^2 = \frac{1}{2}\sin^2\left(\frac{1}{2}(\beta \pm \gamma)\right), \qquad (59)$$

where $+$ and $-$ correspond to $\sigma=0$ and $\sigma=1$, respectively, and β and γ are angular constants that depend on the two-particle interaction $\hat{V}$. They describe the linear combination of the dot-electron states $|B\rangle^D$ and $|A\rangle^D$ within the two-particle wave function. The explicit expressions of β and γ do not enter the final result of this section. The expressions in Eq. (59) reflect the fact that the probabilities for the electron in the QWR to be either in state $|0\rangle^W$ or in state $|1\rangle^W$ are equal. The next step consists in applying the phase gate $\hat{P}$ and the second $\pi/2$ rotation gate $\hat{R}$. This procedure yields the final state probability amplitudes

$$E^r_{0,Y} = \frac{1}{\sqrt{2}}[\exp(i\phi)A_{0,Y} + A_{1,Y}],$$

$$E^r_{1,Y} = \frac{1}{\sqrt{2}}[-\exp(i\phi)A_{0,Y} + A_{1,Y}]. \qquad (60)$$

Note that the gates $\hat{R}$ and $\hat{P}$, being single-qubit transformations, do not change the degree of entanglement of the two electrons. For the transmission probabilities T_1 and T_2, we finally obtain

$$T_{1,2} = \frac{1}{2} \pm |A_{0,B}||A_{1,B}|\cos(\phi + \delta_B) \pm |A_{0,A}||A_{1,A}|\cos(\phi + \delta_A), \qquad (61)$$

where the signs $\pm$ correspond to T_1 and T_2, respectively. The phase angles are defined by $\delta_A = \arg(A_{0,A}) - \arg(A_{1,A})$ and analogously for δ_B. By inserting the expressions for $A_{\sigma,Y}$ into Eq. (61), the transmission probabilities read

$$T_{1,2} = \frac{1}{2}\left[1 \pm \sqrt{\cos^2\beta\sin^2\delta + \cos^2\gamma\cos^2\delta}\cos(\phi + \phi_0)\right], \qquad (62)$$

where $\delta = \frac{1}{2}(\delta_B - \delta_A)$ and ϕ_0 is a constant phase shift. This result shows that the transmission probabilities T_1 and T_2 yield a sinusoidal oscillation as a function of the phase angle ϕ. By comparing the definition [Eq. (51)] of the visibility with this result for the transmission probabilities, we see that the visibility can be written in the form

$$v = \sqrt{\cos^2\beta\sin^2\delta + \cos^2\gamma\cos^2\delta}. \qquad (63)$$

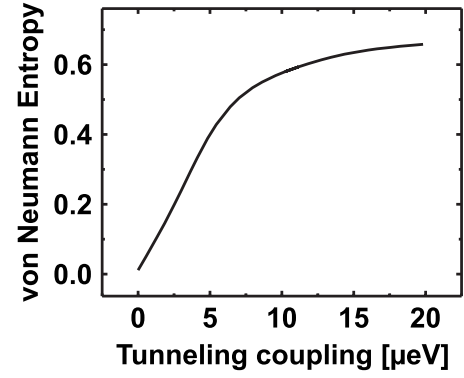Now, we evaluate the expression $|Z|^2 - T_1 T_2$ within Eq. (56) and obtain

FIG. 13. Calculated von Neumann entropy, as defined in the text, of the entangled Mach-Zehnder double quantum dot device of Sec. V C as a function of the tunneling coupling in μeV.

$$|Z|^2 - T_1 T_2 = \frac{1}{4}(\cos^2\beta\sin^2\delta + \cos^2\gamma\cos^2\delta - 1) = \frac{1}{4}(v^2 - 1). \qquad (64)$$

Inserting this result into Eq. (56), we finally obtain the assertion in Eq. (58).

This result proves that the von Neumann entropy of the reduced density matrix depends monotonously on the visibility. A visibility of $v=1$ corresponds to vanishing von Neumann entropy (zero degree of entanglement), while for a visibility of $v=0$, we find a von Neumann entropy of $S=1$ (maximum degree of entanglement). While the relation Eq. (58) between visibility v and von Neumann entropy S may not hold rigorously for the realistic entangled Mach-Zehnder double quantum dot device, it is nevertheless interesting to calculate S for this device as a function of the tunneling coupling, invoking the relation in Eq. (58). The result is presented in Fig. 13 and shows that the degree of entanglement of the realistic device monotonously increases with increasing tunneling coupling.

VI. CONCLUSION

We have theoretically analyzed semiconductor single- and two-qubit quantum gates based on electrostatically defined QWRs and quantum dots. We predict the detailed three-dimensional geometry, material composition, doping profile, and bias voltage of an all-electric Mach-Zehnder interferometer. Our calculations of the electronic structure and ballistic transport properties of this device show that the proposed device is a fully controllable single-qubit gate for electrons that propagate in QWRs. The fabrication of the Mach-Zehnder interferometer is within the reach of present-day technology, but full control of the electronic beam splitters requires a very high fabrication precision in the range of a few nanometers.

Based on this all-electric Mach-Zehnder interferometer, we predict a two-qubit quantum transport device where the electrons in the interferometer couple to a single-electron double quantum dot by Coulomb interaction. We have calculated the ballistic transport properties of the three-

dimensional two-qubit device with an interacting two-particle quantum transport method and designed the device geometry for optimal entanglement. By means of an analytical model of the device, we have illustrated the qualitative physics of the two-qubit device and showed that the visibility is a faithful measure of the entanglement. In particular, we have found that the visibility can be controlled externally by tuning the tunneling coupling between the two quantum dots of the second qubit. The device realizes a nontrivial two-qubit gate that allows the controlled generation and straightforward detection of entanglement from dc current-voltage characteristics.

[1] I. L. Chuang and Y. Yamamoto, Phys. Rev. A **52**, 3489 (1995).

[2] P. Domokos, J. M. Raimond, M. Brune, and S. Haroche, Phys. Rev. A **52**, 3554 (1995).

[3] J. I. Cirac and P. Zoller, Phys. Rev. Lett. **74**, 4091 (1995).

[4] N. Gershenfeld and I. L. Chuang, Science **275**, 350 (1997).

[5] G. K. Brennen, C. M. Caves, P. S. Jessen, and I. H. Deutsch, Phys. Rev. Lett. **82**, 1060 (1999).

[6] D. P. DiVincenzo, Phys. Rev. A **51**, 1015 (1995).

[7] M. A. Nielsen and I. L. Chuang, *Quantum Computation and Quantum Information* (Cambridge University Press, Cambridge, England, 2000).

[8] H. J. Krenner, S. Stufler, M. Sabathil, E. C. Clark, P. Ester, M. Bichler, G. Abstreiter, J. J. Finley, and A. Zrenner, New J. Phys. **7**, 184 (2005).

[9] L. M. K. Vandersypen, M. Steffen, G. Breyta, C. S. Yannoni, M. H. Sherwood, and I. L. Chuang, Nature (London) **414**, 883 (2001).

[10] D. Loss and D. P. DiVincenzo, Phys. Rev. A **57**, 120 (1998).

[11] F. H. L. Koppens, C. Buizert, K. J. Tielrooij, I. T. Vink, K. C. Nowack, T. Meunier, L. P. Kouwenhoven, and L. M. K. Vandersypen, Nature (London) **442**, 766 (2006).

[12] J. R. Petta, A. C. Johnson, J. M. Taylor, E. A. Laird, A. Yacoby, M. D. Lukin, C. M. Marcus, M. P. Hanson, and A. C. Gossard, Science **309**, 2180 (2005).

[13] A. Yacoby, U. Sivan, C. P. Umbach, and J. M. Hong, Phys. Rev. Lett. **66**, 1938 (1991).

[14] A. Bertoni, P. Bordone, R. Brunetti, C. Jacoboni, and S. Reggiani, Phys. Rev. Lett. **84**, 5912 (2000).

[15] R. Ionicioiu, G. Amaratunga, and F. Udrea, Int. J. Mod. Phys. B **15**, 125 (2001).

[16] J. A. del Alamo and C. C. Eugster, Appl. Phys. Lett. **56**, 78 (1990).

[17] P. Pingue, V. Piazza, F. Beltram, I. Farrer, D. A. Ritchie, and M. Pepper, Appl. Phys. Lett. **86**, 052102 (2005).

[18] J. Harris, R. Akis, and D. K. Ferry, Appl. Phys. Lett. **79**, 2214 (2001).

[19] E. Polizzi and N. Ben Abdallah, Phys. Rev. B **66**, 245301 (2002).

[20] G. B. Akguc, L. E. Reichl, A. Shaji, and M. G. Snyder, Phys. Rev. A **69**, 042303 (2004).

[21] A. Marchi, A. Bertoni, S. Reggiani, and M. Rudan, IEEE Trans. Nanotechnol. **3**, 129 (2004).

[22] A. Bertoni, P. Bordone, R. Brunetti, C. Jacoboni, and S. Reggiani, J. Mod. Opt. **49**, 1219 (2002).

[23] R. Ionicioiu, P. Zanardi, and F. Rossi, Phys. Rev. A **63**, 050101(R) (2001).

[24] A. Bertoni, R. Ionicioiu, P. Zanardi, F. Rossi, and C. Jacoboni, Physica B **314**, 10 (2002).

[25] A. Marchi, S. Reggiani, A. Bertoni, and M. Rudan, J. Comput. Electron. **2**, 381 (2003).

[26] L. E. Reichl and M. G. Snyder, Phys. Rev. A **72**, 032330 (2005).

[27] M. G. Snyder and L. E. Reichl, Phys. Rev. A **70**, 052330 (2004).

[28] A. Ramamoorthy, J. P. Bird, and J. L. Reno, Appl. Phys. Lett. **89**, 013118 (2006).

[29] A. Ramamoorthy, J. P. Bird, and J. L. Reno, Appl. Phys. Lett. **89**, 153128 (2006).

[30] S. F. Fischer, G. Apetrii, U. Kunze, D. Schuh, and G. Abstreiter, Nat. Phys. **2**, 91 (2006).

[31] S. F. Fischer, Int. J. Mod. Phys. B **21**, 1326 (2007).

[32] Y. Ji, Y. Chung, S. Sprinzak, M. Heiblum, D. Mahalu, and H. Shtrikman, Nature (London) **422**, 415 (2003).

[33] D. Mamaluy, M. Sabathil, and P. Vogl, J. Appl. Phys. **93**, 4628 (2003).

[34] D. Mamaluy, D. Vasileska, M. Sabathil, T. Zibold, and P. Vogl, Phys. Rev. B **71**, 245321 (2005).

[35] W. G. van der Wiel, S. De Franceschi, J. M. Elzerman, R. Fujisawa, S. Tarucha, and L. P. Kouwenhoven, Rev. Mod. Phys. **75**, 1 (2003).

[36] S. Datta, *Electronic Transport in Mesoscopic Systems* (Cambridge University Press, Cambridge, England, 1995).

[37] M. Büttiker, Phys. Rev. Lett. **57**, 1761 (1986).

[38] *Templates for the Solution of Algebraic Eigenvalue Problems: A Practical Guide*, edited by Z. Bai, J. Demmel, J. Dongarram, A. Ruhe, and H. van der Vorst (SIAM, Philadelphia, 2000).

[39] T. Dupont, R. P. Kendall, and H. H. Rachford, SIAM (Soc. Ind. Appl. Math.) J. Numer. Anal. **5**, 559 (1968).

[40] See http://www.caam.rice.edu/software/ARPACK/ for obtaining the ARPACK libraries and related publications.

[41] A. Trellakis, T. Zibold, T. Andlauer, S. Birner, R. K. Smith, R. Morschl, and P. Vogl, J. Comput. Electron. **5**, 285 (2006).

[42] A. Trellakis, A. T. Galick, A. Pacelli, and U. Ravaioli, J. Appl. Phys. **81**, 7880 (1997).

[43] A. Peres, *Quantum Theory: Concepts and Methods* (Kluwer Academic, Dordrecht 1993).